

# AzTEC Millimetre Survey of the COSMOS Field: I. Data Reduction and Source Catalogue

K.S. Scott,<sup>1</sup> J.E. Austermann,<sup>1</sup> T.A. Perera,<sup>1</sup> G.W. Wilson,<sup>1</sup> I. Aretxaga,<sup>2</sup> J.J. Bock,<sup>3</sup> D.H. Hughes,<sup>2</sup> Y. Kang,<sup>4</sup> S. Kim,<sup>4</sup> P.D. Mauskopf,<sup>5</sup> D.B. Sanders,<sup>6</sup> N. Scoville,<sup>7</sup> and M.S. Yun<sup>1</sup>

<sup>1</sup>*Department of Astronomy, University of Massachusetts, Amherst, MA 01003.*

<sup>2</sup>*Instituto Nacional de Astrofísica, Óptica y Electrónica, Tonantzintla, Puebla, México.*

<sup>3</sup>*Jet Propulsion Laboratory, California Institute of Technology, Pasadena, CA 91109.*

<sup>4</sup>*Astronomy & Space Science Department, Sejong University, Seoul, South Korea.*

<sup>5</sup>*Physics and Astronomy, Cardiff University, Wales, UK.*

<sup>6</sup>*Institute for Astronomy, University of Hawaii, Honolulu, HI 96822*

<sup>7</sup>*California Institute of Technology, Pasadena, CA 91125.*

23 October 2018

## ABSTRACT

We present a 1.1 mm wavelength imaging survey covering 0.3 deg<sup>2</sup> in the COSMOS field. These data, obtained with the AzTEC continuum camera on the James Clerk Maxwell Telescope (JCMT), were centred on a prominent large-scale structure over-density which includes a rich X-ray cluster at  $z \approx 0.73$ . A total of 50 millimetre galaxy candidates, with a significance ranging from 3.5–8.5 $\sigma$ , are extracted from the central 0.15 deg<sup>2</sup> area which has a uniform sensitivity of  $\sim 1.3$  mJy/beam. Sixteen sources are detected with  $S/N \geq 4.5$ , where the expected false-detection rate is zero, of which a surprisingly large number (9) have intrinsic (de-boosted) fluxes  $\geq 5$  mJy at 1.1 mm. Assuming the emission is dominated by radiation from dust, heated by a massive population of young, optically-obscured stars, then these bright AzTEC sources have FIR luminosities  $> 6 \times 10^{12} L_{\odot}$  and star formation-rates  $> 1100 M_{\odot}/\text{yr}$ . Two of these nine bright AzTEC sources are found towards the extreme peripheral region of the X-ray cluster, whilst the remainder are distributed across the larger-scale over-density. We describe the AzTEC data reduction pipeline, the source-extraction algorithm, and the characterisation of the source catalogue, including the completeness, flux de-boosting correction, false-detection rate and the source positional uncertainty, through an extensive set of Monte-Carlo simulations. We conclude with a preliminary comparison, via a stacked analysis, of the overlapping MIPS 24  $\mu\text{m}$  data and radio data with this AzTEC map of the COSMOS field.

**Key words:** galaxies:high-redshift, galaxies:starburst, submillimetre

## 1 INTRODUCTION

A decade after the discovery of a population of extremely luminous, high-redshift dust-obscured galaxies detected by their sub-millimetre and millimetre wavelength emission (Smail et al. 1997; Hughes et al. 1998; Barger et al. 1998), over 200 sub-mm/mm galaxies (hereafter SMGs) have been detected with signal to noise ratio  $\geq 4$  in blank field surveys (e.g., Borys et al. 2003; Greve et al. 2004; Laurent et al. 2005; Coppin et al. 2006) and in surveys towards moderate redshift clusters designed to probe the faintest SMGs via lensing (e.g., Smail et al. 1998, 2002; Chapman et al. 2002). Their high FIR luminosities ( $L_{\text{FIR}} \sim 10^{12-13} L_{\odot}$ ) and in-

ferred star formation rates (SFR  $\gg 100 M_{\odot}/\text{yr}$ , Smail et al. 1997; Hughes et al. 1998; Barger et al. 1998) suggest that these galaxies are high-redshift analogs to the local ULIRG population (Sanders & Mirabel 1996), and that they may be the progenitors of the massive elliptical population observed locally.

Until recently, the relatively modest mapping speeds of SCUBA (850  $\mu\text{m}$ , Holland et al. 1999) on the 15-m James Clerk Maxwell Telescope (JCMT), MAMBO (1.2 mm, Kreysa et al. 1998) on the Institut de Radio Astronomie Millimétrique (IRAM) 30-m telescope and Bolocam (1.1 mm, Glenn et al. 1998; Haig et al. 2004) on the 10-m Caltech Submillimeter Observatory (CSO), have restricted SMG sur-

veys to  $< 300$  arc-min<sup>2</sup> in size, limiting our understanding of the brightest, rarest SMGs and resulting in wide variations in the derived number counts as a result of small number statistics and cosmic variance (e.g., Chapman et al. 2002; Smail et al. 2002; Scott et al. 2002; Borys et al. 2003). With new emphasis on large ( $> 300$  arc-min<sup>2</sup>) sub-mm/mm blank field surveys, (Greve et al. 2004; Laurent et al. 2005; Mortier et al. 2005; Bertoldi et al. 2007), an accurate characterisation of the bright end of the SMG number counts and the mean properties of the SMG population is now becoming possible (e.g., Coppin et al. 2006).

We surveyed a  $0.15$  deg<sup>2</sup> region within the COSMOS field (Scoville et al. 2007) with uniform sensitivity at  $1.1$  mm with the AzTEC camera (Wilson et al. 2008) on the JCMT. The AzTEC survey field is centred on a prominent large-scale structure as traced by the galaxy density (Scoville et al. 2007), including a massive galaxy cluster at  $z = 0.73$  (Figure 1). This AzTEC map has no overlap with the MAMBO/COSMOS survey (Bertoldi et al. 2007) and only a small amount of overlap with the shallower Bolocam survey (J. Aguirre, private communication). Both MAMBO and Bolocam surveys cover a low galaxy-density region of the COSMOS field, whilst our new AzTEC observations are designed to examine the impact of massive large-scale foreground structures on SMG surveys in order to provide a measure of the importance of cosmic variance in the observed source-density at millimetre wavelengths.

In this paper we present the AzTEC mm survey of the COSMOS field, including the data reduction and source catalogue. Since this is the first in a series of papers describing the surveys completed by AzTEC on the JCMT, we provide an extensive description of the data analysis pipeline used to extract sources from AzTEC maps. The JCMT observations, pointing, and calibration strategy are described in § 2. A detailed description of the data reduction algorithm is given in § 3. In § 4, we present the AzTEC map and source catalogue, followed by a discussion of simulations used to determine flux boosting, false-detection rate, completeness, and source positional uncertainty in the map in § 5. A preliminary comparison of the mm sources to the radio and MIPS  $24$   $\mu$ m populations is made in § 6, and we discuss the contribution of AzTEC sources to the Cosmic Infrared Background in § 7.

The large number of bright SMGs identified in the AzTEC/COSMOS field strongly suggests a bias in the number density introduced by the known large-scale structure that is present in the map. A detailed treatment of this analysis is beyond the scope of this paper and is deferred to Paper II (Austermann et al., in prep.). The multi-wavelength imaging data from the HST/ACS, *Spitzer* IRAC and MIPS, as well as deep radio imaging from the VLA is particularly valuable for identifying and studying the nature of the SMGs identified by AzTEC. We will present a complete study of the multi-wavelength properties of the SMGs detected in the COSMOS field in Paper III.

We assume a flat  $\Lambda$ CDM cosmology with  $\Omega_M = 0.3$ ,  $\Omega_\Lambda = 0.7$ , and  $H_0 = 73$  km s<sup>-1</sup> Mpc<sup>-1</sup> throughout.

## 2 OBSERVATIONS

We selected a  $0.3$  deg<sup>2</sup> region in the northwest quadrant of the COSMOS field for millimetre imaging with AzTEC. Only the central area of  $0.15$  deg<sup>2</sup>, with uniform noise, is discussed in this paper. The observations were carried out at the JCMT in November and December 2005. A total of 34 hours of telescope time (excluding pointing and calibration overheads) was devoted to this survey.

Details of the AzTEC instrument specifications, performance, and calibration method at the JCMT are described in Wilson et al. (2008) and are briefly summarised here. The array field of view is roughly circular with a diameter of  $5'$ . During the JCMT observing campaign, 107 out of the 144 detectors were operational. The point spread function (PSF) of the detectors is determined from beam map observations on bright point sources and is well described by a two-dimensional Gaussian, with a beam FWHM of  $17'' \pm 1''$  in Azimuth and  $18'' \pm 1''$  in Elevation.

The COSMOS data-set consists of 34 individual raster-scan observations, each centred at (RA, DEC) = ( $10^{\text{h}}00^{\text{m}}00^{\text{s}}$ ,  $+02^{\circ}36'00.0''$ ). The observations were taken in unchopped raster-scan mode by sweeping the telescope in Elevation, taking a small step of  $10''$  in Azimuth, then sweeping back in the opposite direction, moving only the primary dish. This pattern is repeated until the entire field has been mapped. The small step size ( $\sim 1/2$  the beam FWHM) and chosen scan speeds result in a Nyquist-sampled sky with extremely uniform coverage for each individual observation.

The first half of the observations were taken early in the JCMT observing run, while scanning strategies were still being optimised. For these observations, we imaged a  $25 \times 25$  arc-min<sup>2</sup> region, using a scan speed of  $90''/s$ . From diagnostic tests of these early AzTEC/JCMT observations, we determined that a faster scan speed of  $150''/s$  was optimal, since scanning the camera faster moves the point-source response to higher temporal frequencies and away from the low-frequency atmospheric signal, improving the effectiveness of our cleaning algorithm (Wilson et al. 2008). The time necessary to turn the telescope around between scans (i.e. reverse direction) is constant and independent of scan speed. Therefore, to maintain observational efficiency, we expanded the survey region to  $30 \times 30$  arc-min<sup>2</sup> for the later observations

Since the array orientation is fixed in Azimuth and Elevation, the scan angle in the RA-DEC plane for a raster-scan map continuously changes due to sky rotation. When combining several observations with different scan angles into a single map, we obtain excellent cross-linking that suppresses scan-synchronous systematic noise in the maps. We chose to scan in the Elevation direction rather than in Azimuth to avoid vibrational noise from the telescope dome motion (Wilson et al. 2008).

The opacity at  $225$  GHz,  $\tau_{225}$ , was recorded every 10 minutes by the CSO tau monitor. For the AzTEC/COSMOS observations, the effective opacity,  $\tau_{225} \cdot A$ , where  $A$  is the airmass, ranged from  $0.07$ – $0.27$  with an average value of  $0.15$ . The empirical mapping speed (excluding overheads) derived from the individual COSMOS observations ranges from  $8$ – $34$  arc-min<sup>2</sup> mJy<sup>-2</sup> hr<sup>-1</sup> and is a strong function of  $\tau_{225} \cdot A$  (Wilson et al. 2008), suggesting that the noise in each individual observation is dominated by residual atmosphere

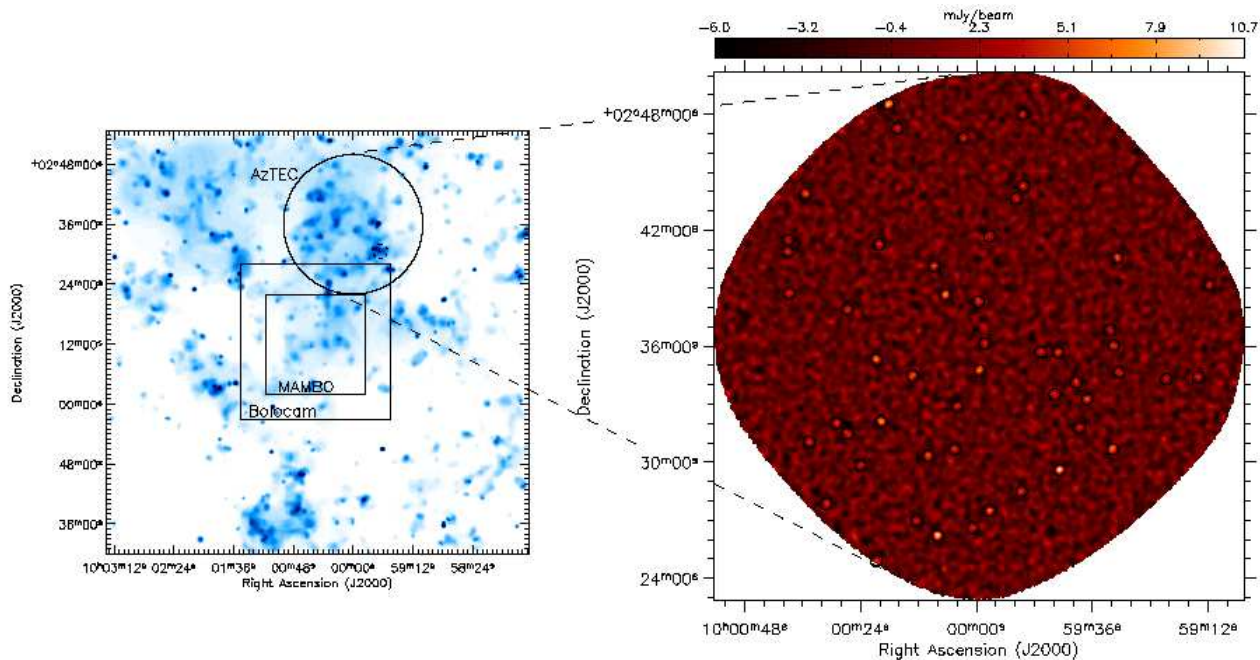


**Figure 1.** **Left:** The galaxy density map from Scoville et al. (2007), with the boundaries of the AzTEC, Bolocam, and MAMBO mm surveys within the COSMOS field indicated. The location of the  $z = 0.73$  cluster environment is identified by the dashed circle. **Right:** The AzTEC/COSMOS map with  $\geq 3.5\sigma$  source candidates identified by circles with diameters equal to twice the AzTEC FWHM on the JCMT. The map has been trimmed to the “75% coverage region” and has an average rms noise level of 1.3 mJy/beam and an area of  $0.15 \text{ deg}^2$ . The signal map has been Wiener filtered for optimal identification of sources as described in § 3.5.

that is not removed in the cleaning process. We discuss the details of atmosphere removal and optimal filtering in the next section.

## 2.1 Pointing

Observations of J1058+015, a variable QSO with a mean flux density of 2.8 Jy, were made approximately every two hours in order to generate small corrections to the JCMT’s pointing model. These corrections were not made in real time. Instead, a correction based on a linear interpolation of the measured pointing offsets was applied to each observation *ex post facto*. In § 6.2 we demonstrate that the resulting absolute pointing uncertainty of the AzTEC map is  $< 2''$ .

## 2.2 Flux Calibration

The AzTEC calibration has been derived from beam map observations of Uranus, which had a predicted flux density of 44.3–48.5 Jy at 1.1 mm during the JCMT observing run. We fit a two-dimensional Gaussian to the PSF of each detector to determine the flux conversion factor (FCF) from optical loading (in Watts) to source flux (in Jy/beam). Beam maps were taken once per night. The extinction- and responsivity-corrected FCF for each detector did not vary greatly over the entire observing run. We use an average FCF for each bolometer determined from all Uranus beam maps taken at the JCMT. The total error of 6–13% on the calibrated signals includes the standard deviation of the measured FCFs plus errors from the extinction and responsivity corrections (Wilson et al. 2008). This value does not include

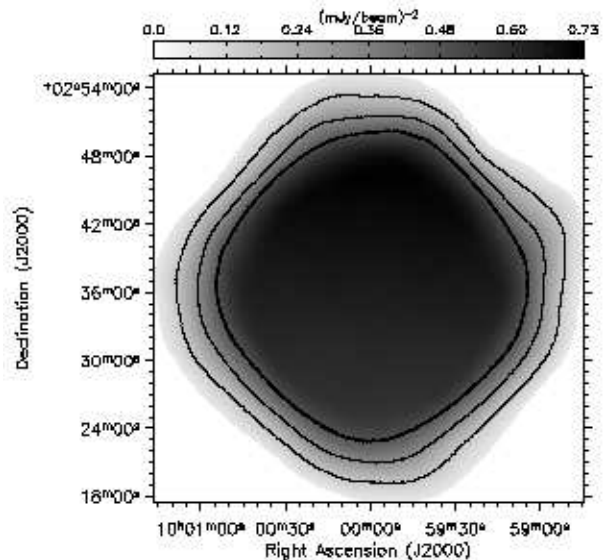


**Figure 2.** The weight map for the AzTEC/COSMOS survey. The contours show curves of constant noise and are 1.4, 1.8, and 2.5 mJy/beam from the innermost to the outermost contour. The thick, innermost contour indicates the  $0.15 \text{ deg}^2$  “75% coverage region” where the signal map is trimmed to provide very uniform coverage in the region where the analysis in this paper is carried out. The noise levels in this central region of the map range from 1.2 to 1.4 mJy/beam.

the 5% absolute uncertainty in the flux density of Uranus (Griffin & Orton 1993). The data are calibrated after atmosphere removal and before combining the time-stream signals from all bolometers into a single map.

### 3 DATA REDUCTION

The AzTEC/COSMOS data-set is reduced using the publicly available AzTEC Data Reduction Pipeline V1.0 written in IDL and developed by AzTEC instrument team members at the University of Massachusetts, Amherst. V1.0 has been optimised for the identification of point sources in blank-field extragalactic surveys. The 34 individual raster-scan observations that comprise the AzTEC/COSMOS data-set are ultimately combined to produce four data products: 1) a co-added signal map; 2) a corresponding weight map; 3) a set of noise maps which are representative of the noise in the co-added signal map; and 4) a representation of the instrument point source response, post-cleaning and filtering. We describe the techniques for creating these data products from raw AzTEC data in detail in this section.

The raw data-file for each raster-scan observation is composed of bolometer signals, telescope pointing signals, and environmental signals – all stored as a function of time and referred to hereafter as “time-stream” data. Detector signals are sampled at a rate of 64 Hz and all germane environmental signals are interpolated to this sampling rate in the analysis. In the description below, a “scan” is defined as a single constant-velocity and constant-Elevation pass of the telescope from one side of the field to the other. We do not use the data recorded as the telescope is strongly accelerating at the ends of the scans (during the turn-around), where the accuracy of the pointing signals is unknown and micro-phonic noise is more likely. Given the field size and scan velocities used for the AzTEC/COSMOS survey, this results in a loss of 22–34% of the on-source observing time.

#### 3.1 De-spiking

Prior to atmosphere removal, the data are inspected for cosmic ray events and instrumental glitches, both of which register as “spikes” in the raw time-stream data. Spikes in the AzTEC data occur at a rate of  $\sim 40 \text{ hr}^{-1}$ , each usually confined to a single detector, and with amplitudes that vary widely from 30 mJy to 550 Jy. Spikes are defined in our automated spike identification and removal procedure as any instance where a detector signal jumps by a user-defined threshold (typically  $> 7\sigma$  or  $< -7\sigma$ ) between adjacent time samples. Generally, such jumps in detector output cannot be of astronomical origin as the continuous nature of the beam and the scanning strategy ensure a smoother signal. Spikes are located recursively, thus allowing for pairs of spikes with high dynamic range to be identified independently. A spike decay length (time necessary for the spike signal to drop below the baseline noise rms) is calculated based on the spike amplitude and a conservative estimate of the detector time constant. Adjacent samples are flagged accordingly, with a minimum of 12 (6) samples flagged after (before) the spike. Flagged data samples are not included in the map-making process. For the AzTEC/COSMOS data-set, flagged sam-

ples due to spikes account for  $< 0.1\%$  of the total time-stream data.

Since the matrix operations in our atmosphere removal technique requires that all bolometers have the same number of time-stream samples, we cannot simply discard the flagged samples. Large spikes can affect upwards of  $\sim 20$  adjacent time samples for a single detector and de-correlate that detector’s time stream from the remainder of the array. Unaccounted for, this would reduce the efficacy of the atmospheric cleaning technique and so we replace each set of flagged samples with the sum of two components: 1) Gaussian noise with variance equal to the variance of that detector’s time-stream from nearby unflagged samples; and 2) an appropriately scaled baseline calculated from the mean time-stream for all unaffected detectors. In this manner, the detector-detector covariance matrix is minimally affected and, more importantly, the inclusion of noise ensures that excess weight is not given to the synthetic time-stream samples. These simulated data are used *only* in the atmosphere removal process; all flagged samples are discarded when making the actual map.

#### 3.2 Atmosphere Removal

The signal due to the fluctuating atmosphere dominates the background SMG population by three orders of magnitude. For the AzTEC/COSMOS data-set and other “blank-field” surveys we adopt an adaptive principal component analysis (PCA) technique similar to that described by Laurent et al. (2005) to remove, or “clean” the correlated sky noise from the time-stream data. Faint point sources are, in general, not correlated between detectors in the array while the atmosphere is correlated on all spatial scales of interest. The adaptive PCA technique uses the degree of correlations to distinguish between the two.

Cleaning is accomplished on a scan by scan basis. The basic adaptive PCA cleaning process is as follows: a covariance matrix is constructed from the  $N_{\text{bolo}}$  by  $N_{\text{time}}$  de-spiked time-stream data for each scan and then eigenvalue decomposed. The relative amplitudes of the resulting eigenvalues are representative of the degree of correlation of the detector signals for the mode described by the respective eigenvector. Since fundamental detector noise and faint point sources are not correlated amongst multiple detectors, they will not lie preferentially in modes having large eigenvalues. The atmosphere, fluctuations in the detector bias chain, and other common-mode signals dominate the correlated variance with their power in modes with large eigenvalues. The technique, then, is to identify and project out modes with the largest eigenvalues.

The choice of which modes to remove from the data is somewhat arbitrary. Empirically we have found the following to work well. First, the mean and standard deviation in the base-10 logarithm of the eigenvalue distribution is determined, then large eigenvalues that are  $> 2.5\sigma$  from the mean are cut. This process is repeated until no  $> 2.5\sigma$  outliers exist. An example of the time stream data and power spectral density (PSD) before and after PCA cleaning is shown in Figure 3. The significant decrease in the power at low frequencies demonstrates how this adaptive PCA cleaning technique effectively removes much of the atmospheric signal.

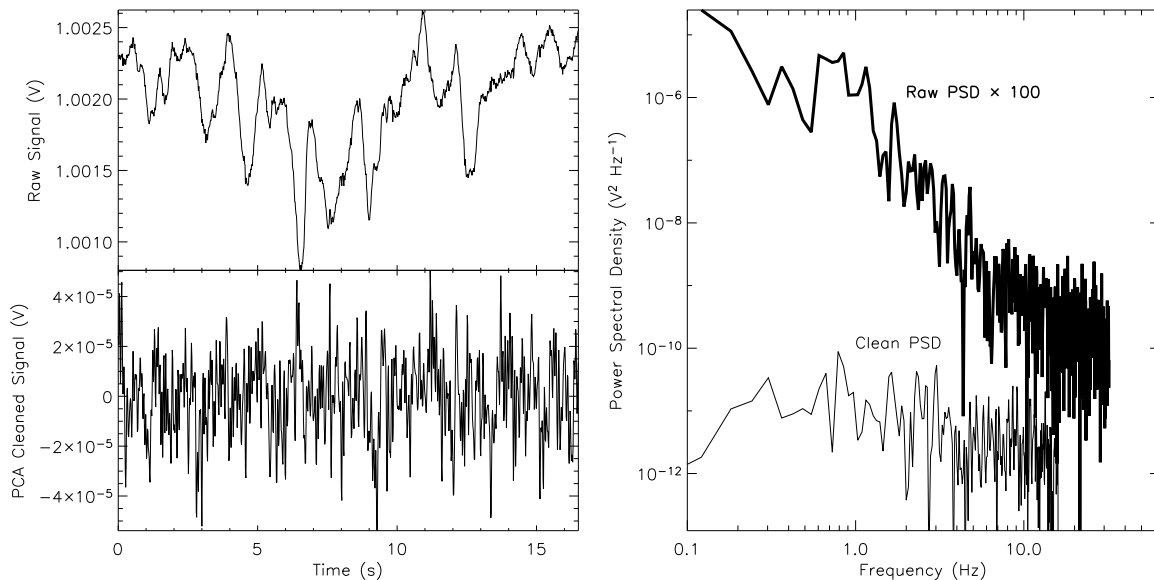


**Figure 3. Top Left:** The raw time-stream signals for a sample bolometer during a single scan. **Bottom Left:** The same time-stream signals after PCA cleaning. Note the factor of 20 reduction in the noise level post-cleaning. **Right:** The power spectral density (PSD) of the same scan, before (thick) and after (thin) PCA cleaning, demonstrating the reduction of low-frequency signal. The PSD before PCA cleaning has been multiplied by a factor of 100 to offset the two curves. The PSD of the post-cleaned data is truncated at 16 Hz due to a digital low-pass filter that is applied to the data before PCA cleaning.

There are two consequences of the adaptive PCA technique that must be addressed. First, since faint point sources have power at low spatial frequencies, there is no way to completely decouple the atmosphere from the point source signal. We therefore expect some attenuation of point sources in the resulting map. Secondly, PCA cleaning decouples the time-stream signal, leaving the mean of the samples for each bolometer in a single scan equal to zero.

We trace the effects of PCA cleaning on the point source response profile and its amplitude to generate the point source kernel, which we use later in the analysis to optimally filter the map and correct for the attenuation. Since the degree of attenuation varies according to the conditions of the atmosphere for a given observation, we create a point source kernel for each observation separately. The procedure is as follows: 1) each scan of an observation is cleaned according to the prescription given above, saving the set of eigenvalues and eigenvectors for later use; 2) an analogous, synthetic time-stream is created using the pointing signals to make a fake “observation” of a 1 Jy point source centred in an otherwise empty and noiseless field. The flux of the synthetic point source is arbitrary – we only need to determine the factor of attenuation and the effect that PCA cleaning has on the shape of the point source response; 3) the dominant eigenvectors identified in 1) are projected out from the synthetic data; and 4) a map is made from this cleaned, synthetic data. The resulting image is the point source kernel, and it has the same shape and attenuation as a point source in the cleaned signal map for a given observation. This is true only if the real sources in the time-stream signal do not significantly affect the PCA cleaning, and if the kernel does not vary greatly in shape and attenuation across the whole field. The standard deviation and spatial PSD of an individual signal map is comparable to that in

a jackknifed noise realisation of that map (see § 3.4), which suggests that the former must be true. We have tested the latter assumption by placing the synthetic 1 Jy point source at different locations in the field. We find that the shape of the kernel is not affected by its location, and the measured peak of the PCA-cleaned kernel varies by less than 2% over the entire field.

In Figure 4, we show a cut in Elevation through the synthetic point source for one of the observations, before and after PCA cleaning. This demonstrates the attenuation that a real source experiences from the atmosphere removal process. In this case, the sources will be attenuated by 17.8% due to PCA cleaning. This also shows how the cleaning affects the shape of point sources. The central peak is now flanked with negative side-lobes and has a small negative baseline that extends across the map, making the mean of the point source response equal to zero.

### 3.3 Raw Signal Maps

We cast each of the 34 individual raster-scan observations into map space prior to co-adding them into a single map. Hereafter, we will refer to any maps that are made for a single observation as an “individual” map. To ensure that all of these individual maps will have the same coordinate grid, we convert the time-stream pointing signals into offset positions relative to the map centre at (RA, DEC) =  $(10^{\text{h}}00^{\text{m}}00^{\text{s}}, +02^{\circ}36'00'')$ . These pointing signals are then binned into  $2 \times 2$  arc-sec<sup>2</sup> pixels, creating the underlying coordinate grid for the map. We chose 2'' pixelization in order to avoid significant dilution of the peak signal from point sources while maintaining a statistically sufficient number of samples ( $\geq 9$ ) in each pixel. The map value for pixel  $j$  in observation  $i$ ,  $S_{i,j}$ , is calculated from the weighted av-

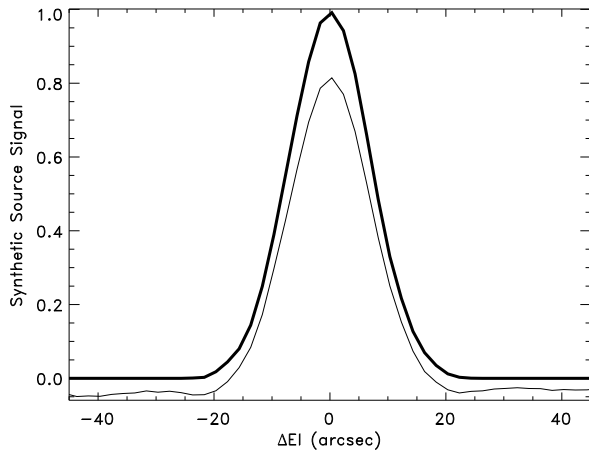


**Figure 4.** A cut in Elevation of the point source kernel for an individual observation. The thick curve shows the effective PSF (once all bolometer signals are combined) *before* PCA cleaning. The thin curve shows the resulting point source response function after the synthetic source has been PCA cleaned in the same manner as the real time-stream signals.

erage of all samples whose central pointing falls within the pixel boundary, combining the samples from all bolometers simultaneously and excluding any samples flagged in the de-spiking process. The weight of each sample is taken to be the inverse variance of the respective detector’s samples in the parent scan. This weighting scheme is only suitable for cases where the source signal is consistent with noise for a single scan observation, which is true for the entire AzTEC/COSMOS data-set.

For each individual COSMOS map,  $S_i$ , we also make the corresponding individual “weight map”,  $W_i$ , by adding in quadrature the weights of all bolometer samples that contribute to a pixel. As the flux assigned to a pixel is a weighted average of these samples, the weight of a pixel is proportional to  $\sigma_i^{-2}$  of the flux estimate. The proportionality constant may differ from unity because all samples contributing to a pixel may not be completely independent, for instance due to detector-detector correlations resulting from imperfect atmosphere removal. However, because the scan strategy and analysis technique are essentially identical for all observations, we expect on average that this proportionality constant is identical over the 34 individual observations and over all pixels of an individual map. As noted before we also make an image of the point source kernel,  $K_i$ , for each individual observation.

We combine all individual COSMOS observations into a single image by computing for each pixel the weighted average over the individual maps:

$$S = \frac{\sum_{i=1}^{34} W_i S_i}{\sum_{i=1}^{34} W_i}. \quad (1)$$

As with each of the individual observations, we also produce the weight map,  $W$ , corresponding to this co-added signal map and an averaged point source kernel,  $K$ .

### 3.4 Noise Maps

With the construction of  $S$ ,  $W$ , and  $K$  we have most of the raw ingredients for making the final map. In order to optimally filter  $S$ , however, we must construct an estimate of the noise in  $S$ . We do this by generating “jackknifed” noise realisations for each COSMOS observation. This is accomplished by multiplying each scan in the cleaned time-stream data by  $\pm 1$  (chosen at random) before the map-making process. This removes the sources, both resolved and confused, from the bolometers’ signals while preserving the noise properties in the individual scans. We then combine jackknifed noise realisations made from each of the 34 observations in the same manner as for the real individual maps to create a single co-added noise map,  $N$ . We choose to jackknife on single-scan scales to ensure a statistically significant number of elements (there are 150–200 scans per observation) and to ensure nearly equal weightings in the positive and negative components while conserving low-frequency components (each scan is  $> 10$  seconds and  $\geq 25'$  in length). This was tested against the more traditional approach to jackknifing, where half the original individual signal maps are multiplied by a factor of  $-1$  before combining the full data-set, which gave consistent results.

For the AzTEC/COSMOS data-set we create five jackknifed noise realisations for each of the 34 COSMOS observations. To verify that these noise realisations are consistent with the noise in the individual signal maps, we compare the standard deviation and the spatial PSD of the noise realisations to those in the raw individual signal maps directly. This test is valid since the contribution from real sources in the individual signal map for a single observation is negligible. We find that the difference between the standard deviations of the individual signal maps and their jackknifed noise realisations is less than 0.6% for every observation. We use random combinations of these noise realisations, one representing each individual observation at a time, to generate a total of 100 co-added noise maps for the field - each a realisation of the underlying noise in the co-added signal map,  $S$ . As described below, these noise maps are used in creating the optimal point source filter for the co-added signal map, and as the underlying noise in synthetic source maps.

### 3.5 Optimal Filtering

At this stage in the analysis, pixel-to-pixel signal variations stand out prominently in the co-added signal map. These variations are not of astronomical origin as the pixel size,  $2''$ , is much smaller than the AzTEC beam. One way to filter out such features is to convolve the signal map with our co-added point source kernel,  $K$ . The resulting map must then be scaled to account for attenuation of the kernel from PCA cleaning. If the noise covariance matrix of the signal map were diagonal, that is, if the errors in the pixel values were independent, then this two-step procedure would be mathematically equivalent to a fitting procedure: that of shifting the centre of  $K$  to the centre of each pixel in  $S$  and fitting it to the signal map to find a best-fit amplitude. The  $K$ -convolved scaled map is equivalent to a map of those best-fit amplitudes. This analogy to fitting is useful since it provides guidance on generalising the filter/convolution procedure and on propagating the error/weight map.

The presence of excess long wavelength noise in the Fourier transform of noise maps is clear evidence of pixel-pixel noise correlations. We de-weight these long wavelength modes by filtering the signal map with the inverse of the square root of the power spectral density, averaged over the 100 noise maps. This filter makes the noise power flat with frequency or, equivalently, removes pixel-pixel correlations in the filtered map. This “whitening” filter is applied to both the signal map and the point source kernel. At this point, a linear convolution of the two is the same as fitting the whitened kernel to the whitened map *assuming a uniform uncertainty for all pixel values*. Such a fit/convolution is equivalent to the conventional “optimal filtering” procedure used by other groups (e.g., Laurent et al. 2005), but we follow the fit analog to completion by including non-uniform coverage as non-constant error values in the fit.

The proper accounting of non-uniform coverage is important for two reasons. First, implicit to such map-making and filtering procedures is the assumption that the sky as seen by AzTEC can be described by a set of discrete points - the centres of the map pixels. For large pixel sizes, this assumption is invalid and results in fluxes (e.g. from point sources) being smoothed out. Therefore, we would like to explore the use of small pixel sizes. While raster-scan maps made with AzTEC have rather uniform coverage on beam scales, the coverage has non-uniformity on small scales like 2". Some groups (e.g., Coppin et al. 2006) seek an “optimal” pixel size that is small enough to avoid flux-smoothing effects and large enough for the coverage variations between pixels to be negligible. But such an optimum may not exist. By including variations in coverage as variable error values in a fitting procedure, we circumvent having a lower limit to the pixel size, save for practical CPU time considerations. Empirically, we have found that pixel sizes below 3" yield essentially the same results in terms of fluxes and sources recovered in AzTEC/JCMT maps.

Second, the error values are formed from our estimate of the uncertainty of each pixel value. Thus, our estimate of the sky coverage of each pixel is correctly propagated through the analysis, resulting in a new weight map that represents the formal weight in the best-fit amplitudes at each pixel. In summary, the optimal filter consists of 1) finding the best-fit amplitude from fitting a whitened point-source kernel to every pixel of a whitened signal map with proper account for the uncertainty of each pixel value, and 2) propagating the weights to yield a new weight map representing the uncertainty in the best-fit amplitude at each pixel. The signal map times the square root of this weight map represents the signal to noise for each pixel.

The above filtering procedure is implemented with linear convolutions, made quicker by the use of fast Fourier transforms. In the optimal filter, a rotationally symmetrized version of the point-source kernel is used. This is a better approximation to point sources over the entire map than the raw kernel averaged over individual observations, which has scan-oriented artifacts that are relevant only to a particular central region of the map. We also make use of noise maps to avoid lengthy calculations and to find an absolute normalisation factor for values in the final weight map. The mathematical formulation of this optimal filter and the details of its implementation will be presented in a future work.

#### 4 SOURCE CATALOGUE

The AzTEC/COSMOS signal map and its weight map are shown in Figures 1 and 2. The signal map shown has been trimmed such that only pixels with weights  $\geq 75\%$  of the map’s characteristic (roughly the maximum) weight are included. This results in a nearly circular map with total area 0.15 deg<sup>2</sup> and very uniform noise across the map, ranging from 1.2 mJy/beam in the centre to 1.4 mJy/beam at the edges of the map. Unless otherwise stated, we limit our analysis to this “75% uniform coverage region”.

Figure 5 shows the histogram of the pixel flux density values in the map. The averaged histogram of pixel values from the filtered noise maps, which is well-fit by a Gaussian with  $\sigma = 1.3$  mJy/beam, is also shown for comparison. There is a clear excess of positive flux pixels in the signal map compared to the noise maps, indicating the presence of both bright and confused sources. The presence of real sources in the map also produces an excess of hot *negative* flux pixels over that expected from Gaussian random noise due to the fact that our map is AC-coupled with a mean of zero. Each source in the map is a scaled version of the point source kernel and contributes excess negative signal due to the negative side-lobes surrounding the central peak (see Figure 4). Real sources change the distribution of flux values in the map from that expected of pure Gaussian noise by skewing the flux distribution (making it very non-Gaussian), broadening the distribution, and shifting the peak to  $< 0$ .

Bright source candidates are identified in the signal to noise map as local maxima within an 18" window above a signal to noise ( $S/N$ ) threshold of 3.5. We find that reducing the “single-source” window from 18" to 4" results in the same number of source detections. While none of these sources are visually extended, it is possible that some of our individually-detected sources consists of multiple components blending together due to the large beam of the instrument. We could attempt to “de-blend” detected sources by fitting them to a combination of two (or more) point source kernels, but this is precluded by the low signal to noise of the detections that makes it difficult to distinguish

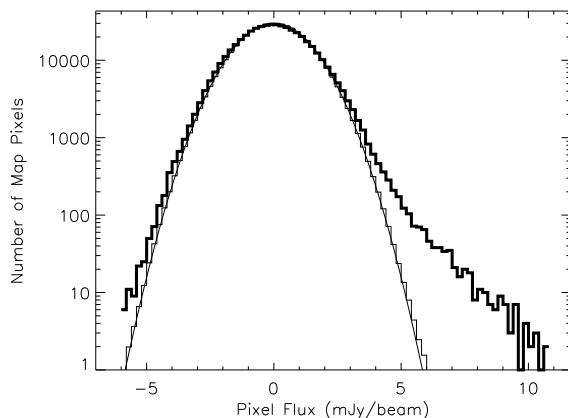


**Figure 5.** Histogram of fluxes from the signal map (thick line) and the average histogram of fluxes from the noise maps (thin line) with the best-fit Gaussian over-plotted. A clear distortion of the map pixel flux values from that expected from noise is seen in the signal map due to the presence of real sources.

between a single source versus multiple blended sources. Sub-pixel centroiding of the source coordinates is calculated by weighting the pixel positions within a  $9''$  radius of the brightest pixel by the flux squared. This method results in a list of 50 source candidates with  $S/N \geq 3.5$ , which are listed in Table 1. The measured flux density for a source is given by the map value at its peak, and the error on the flux density by the noise in that pixel. Note that the optimal filter correctly scales the flux values in the map to account for the flux attenuation arising from PCA cleaning. The “de-boosted” 1.1 mm fluxes for the AzTEC/COSMOS source candidates listed in Table 1 represent the maximum likelihood flux density using the semi-Bayesian approach outlined in the following section.

We find a large number of very bright, high-significance sources in our map, 9 of which have intrinsic fluxes  $\geq 5$  mJy. Assuming a modified blackbody spectral energy distribution (SED) with dust temperature  $T_d = 40$  K and emissivity  $\beta = 1.6$ , these very bright AzTEC galaxies have  $L_{FIR} > 6.0 \times 10^{12} L_\odot$ . Assuming that all of the bolometric output arises from star formation and the relationship between SFR and  $L_{FIR}$  for starburst galaxies from Kennicutt (1998), this implies SFRs  $> 1100 M_\odot/\text{yr}$ . Seven of these sources have been followed-up with interferometric imaging at  $890 \mu\text{m}$  using the Submillimeter Array (SMA) (Younger et al. 2007). All of these sources were detected with the SMA with signal to noise  $\geq 6$  (see Table 1), confirming the reality of these sources and providing  $0.2''$  positional accuracy. With the  $2''$  resolution of the SMA, none of these seven SMGs were resolved into multiple components, implying physical sizes of  $< 16$  kpc at  $z = 2.2$  (the median redshift of SMGs from Chapman et al. 2005) and  $< 13$  kpc at  $z > 4$ , where a fraction of these SMGs are likely to exist based on their faintness or non-detection in the radio (Younger et al. 2007).

From the 1.1 mm number counts of Laurent et al. (2005), we expect on average only 4–5 sources with intrinsic flux density  $\geq 5$  mJy in a blank, unbiased field of this size, compared to the 9 discovered in the AzTEC/COSMOS map. Our map deliberately surveys a biased portion of the COSMOS field (Figure 1) by being centred on prominent large-scale structure as traced by the galaxy density map of Scoville et al. (2007), and there is evidence for a correlation between the positions of the SMGs in the AzTEC map and the projected galaxy density for galaxies with  $z \leq 1.1$  (Austermann et al., in prep. – Paper II). However, for all seven SMGs detected with the SMA, optical and/or radio/far-IR photometric redshifts place the sources behind the foreground structure at  $z = 0.73$  (Younger et al. 2007). If some or all of the  $\geq 5$  mJy sources are lensed, then the bolometric luminosity and SFR calculated above could be significantly overestimated. In Paper II, we will present a complete analysis of the relationship between the SMG population and the foreground galaxy population, including number counts derived from this study as compared with those from known blank-fields, a study of possible galaxy-galaxy lensing of the bright AzTEC/COSMOS sources due to the foreground structure, and several quantitative tests of the correlation of the AzTEC sources with the projected galaxy over-density and weak-lensing mass maps.

## 5 SIMULATIONS

With the machinery described in § 3 in place, it is straightforward to determine various characteristics of our signal map and our source identification process via Monte Carlo simulations. We generate synthetic source maps by populating our synthetic noise maps with point source kernel-shaped sources. Depending on the goal of the simulation, sources of a given flux are randomly placed into the signal or noise map one at a time, or entire populations of sources drawn from a parametrised number-density distribution may be randomly distributed (spatially) in a noise map. When appropriate we determine characteristics of our survey with the former method in order to avoid biasing our results with the (weak) prior of the input source distribution.

### 5.1 Flux De-Boosting

Sources with low  $S/N$  are detected at fluxes systematically higher than their intrinsic flux density when the source population increases in number with decreasing flux. This well known but subtle effect (e.g., Hogg & Turner 1998) becomes important when there are far more faint sources, dimmer than the detection flux limit, than there are brighter sources. In this instance it becomes more likely that the numerous dim sources are boosted high by noise than the rarer bright sources are boosted to lower fluxes. This is particularly significant in surveys of SMGs, where detections are almost always at low  $S/N$  ( $< 10$ ) and the intrinsic population is known to have a very steep luminosity distribution (e.g., Scott et al. 2006, and references therein).

For each source candidate we calculate a posterior flux distribution (PFD) which describes the source’s intrinsic flux in terms of probabilities. The PFD is calculated through an implementation of Bayes theorem similar to that used by Coppin et al. (2005, 2006). For an individual source detected with measured flux density  $S_m \pm \sigma_m$ , the probability distribution for its intrinsic flux density  $S_i$  is given by

$$p(S_i|S_m, \sigma_m) = \frac{p(S_i)p(S_m, \sigma_m|S_i)}{p(S_m, \sigma_m)} \quad (2)$$

where  $p(S_i)$  is the prior distribution of flux densities,  $p(S_m, \sigma_m|S_i)$  is the likelihood of observing the data, and  $p(S_m, \sigma_m)$  is a normalising constant. We assume a Gaussian noise distribution for the likelihood of observing the data, where

$$p(S_m, \sigma_m|S_i) = \frac{1}{\sqrt{2\pi\sigma_m^2}} \exp\left(\frac{-(S_m - S_i)^2}{2\sigma_m^2}\right). \quad (3)$$

This assumption is justified by the Gaussian flux distribution observed in jackknifed noise maps (thin line in Figure 5). We use a Schechter function of the form:

$$\frac{dN}{dS} = N' \left(\frac{S}{S'}\right)^{\alpha+1} \exp(-S/S') \quad (4)$$

for the prior of the number counts, which we use to simulate the flux distribution  $p(S_i)$ . We adopt the best-fit parameters to the SCUBA SHADES number counts (Coppin et al. 2006), scaled to 1.1 mm assuming an  $850 \mu\text{m}/1100 \mu\text{m}$  spectral index of 2.7. The parameters for the Schechter function prior are  $N' = 3200 \text{ deg}^{-2} \text{ mJy}^{-1}$ ,  $S' = 1.6 \text{ mJy}$ , and  $\alpha = -2.0$ . While the PFDs will depend on the exact form of

**Table 1.** AzTEC/COSMOS source candidates. The columns give: 1) AzTEC source name; 2) SMA identification; 3) Signal to noise of the detection in the AzTEC map; 4) Measured 1.1 mm flux density and error; 5) De-boosted flux density and 68% confidence interval (§ 5.1); 6) 890  $\mu\text{m}$  flux density and error (Younger et al. 2007); and 7) Probability that the source will de-boost to  $< 0$  (§ 5.1).

Source	SMA ID	S/N	$S_{1.1\text{mm}}$ (measured) (mJy)	$S_{1.1\text{mm}}$ (de-boosted) (mJy)	$S_{890\mu\text{m}}$ (mJy)	$P(S_{1.1\text{mm}} < 0)$
AzTEC_J095942.68+022936.0	AzTEC1	8.3	$10.7 \pm 1.3$	$9.3^{+1.3}_{-1.3}$	$15.6 \pm 1.1$	0.000
AzTEC_J100008.03+022612.1 <sup>a,b</sup>	AzTEC2	7.4	$9.7 \pm 1.3$	$8.3^{+1.3}_{-1.3}$	$12.4 \pm 1.0$	0.000
AzTEC_J100018.25+024830.2 <sup>b,c</sup>	AzTEC7	6.4	$8.8 \pm 1.4$	$7.1^{+1.4}_{-1.4}$	$12.0 \pm 1.5$	0.000
AzTEC_J100006.40+023839.8	AzTEC6	6.3	$7.7 \pm 1.2$	$6.3^{+1.3}_{-1.2}$	$8.6 \pm 1.3$	0.000
AzTEC_J100019.73+023206.0 <sup>b,c</sup>	AzTEC5	6.2	$7.9 \pm 1.3$	$6.5^{+1.2}_{-1.4}$	$9.3 \pm 1.3$	0.000
AzTEC_J100020.71+023518.2 <sup>b</sup>	AzTEC3	5.9	$7.4 \pm 1.2$	$5.9^{+1.3}_{-1.3}$	$8.7 \pm 1.5$	0.000
AzTEC_J095959.33+023445.8 <sup>b,c</sup>		5.7	$7.1 \pm 1.2$	$5.5^{+1.3}_{-1.3}$		0.000
AzTEC_J095957.22+022729.3 <sup>a,e</sup>		5.6	$7.2 \pm 1.3$	$5.8^{+1.3}_{-1.5}$		0.000
AzTEC_J095931.83+023040.2	AzTEC4	5.3	$6.7 \pm 1.3$	$5.2^{+1.3}_{-1.4}$	$14.4 \pm 1.9$	0.001
AzTEC_J095930.77+024034.2 <sup>b</sup>		5.1	$6.2 \pm 1.2$	$4.7^{+1.3}_{-1.3}$		0.001
AzTEC_J100008.80+024008.0 <sup>b,c</sup>		5.1	$6.2 \pm 1.2$	$4.7^{+1.3}_{-1.3}$		0.001
AzTEC_J100035.37+024352.3 <sup>b,c</sup>		4.8	$6.1 \pm 1.3$	$4.5^{+1.3}_{-1.5}$		0.003
AzTEC_J095937.04+023315.4 <sup>b,c</sup>		4.8	$6.0 \pm 1.3$	$4.4^{+1.3}_{-1.4}$		0.003
AzTEC_J100010.00+023020.0		4.7	$6.0 \pm 1.3$	$4.3^{+1.4}_{-1.4}$		0.005
AzTEC_J100013.21+023428.2 <sup>b</sup>		4.6	$5.8 \pm 1.3$	$4.2^{+1.3}_{-1.3}$		0.005
AzTEC_J095950.29+024416.1		4.5	$5.4 \pm 1.2$	$3.9^{+1.3}_{-1.3}$		0.006
AzTEC_J095939.30+023408.0 <sup>b,c</sup>		4.4	$5.4 \pm 1.2$	$3.8^{+1.4}_{-1.4}$		0.011
AzTEC_J095943.04+023540.2		4.3	$5.4 \pm 1.2$	$3.8^{+1.3}_{-1.5}$		0.012
AzTEC_J100028.94+023200.3 <sup>b,c</sup>		4.3	$5.4 \pm 1.3$	$3.8^{+1.3}_{-1.6}$		0.016
AzTEC_J100020.14+024116.0 <sup>b,c</sup>		4.3	$5.2 \pm 1.2$	$3.6^{+1.3}_{-1.4}$		0.014
AzTEC_J100002.74+024645.0 <sup>b</sup>		4.2	$4.9 \pm 1.2$	$3.4^{+1.3}_{-1.4}$		0.016
AzTEC_J095950.69+022829.5 <sup>b,c</sup>		4.2	$5.4 \pm 1.3$	$3.6^{+1.5}_{-1.6}$		0.022
AzTEC_J095931.57+023601.5 <sup>b</sup>		4.1	$5.1 \pm 1.2$	$3.4^{+1.4}_{-1.5}$		0.021
AzTEC_J100038.72+023843.8 <sup>b,c</sup>		4.1	$5.0 \pm 1.2$	$3.3^{+1.4}_{-1.5}$		0.024
AzTEC_J095950.41+024758.3 <sup>b</sup>		4.1	$4.9 \pm 1.2$	$3.3^{+1.4}_{-1.4}$		0.024
AzTEC_J095959.59+023818.5		4.0	$5.0 \pm 1.2$	$3.3^{+1.4}_{-1.5}$		0.027
AzTEC_J100039.12+024052.5 <sup>b</sup>		4.0	$5.0 \pm 1.2$	$3.3^{+1.4}_{-1.6}$		0.028
AzTEC_J100004.54+023040.1 <sup>b,c</sup>		4.0	$5.1 \pm 1.3$	$3.3^{+1.5}_{-1.6}$		0.035
AzTEC_J100026.68+023753.7		4.0	$4.9 \pm 1.2$	$3.3^{+1.4}_{-1.6}$		0.032
AzTEC_J100003.95+023253.8		4.0	$5.0 \pm 1.3$	$3.3^{+1.4}_{-1.6}$		0.036
AzTEC_J100034.59+023102.0		3.9	$5.0 \pm 1.3$	$3.1^{+1.5}_{-1.6}$		0.040
AzTEC_J100020.66+022452.8 <sup>b</sup>		3.8	$5.4 \pm 1.4$	$3.1^{+1.7}_{-2.0}$		0.071
AzTEC_J095911.76+023909.5		3.8	$5.0 \pm 1.3$	$3.0^{+1.6}_{-1.8}$		0.060
AzTEC_J095946.66+023541.9 <sup>b,c</sup>		3.7	$4.6 \pm 1.2$	$2.8^{+1.5}_{-1.7}$		0.056
AzTEC_J100026.68+023128.1		3.7	$4.8 \pm 1.3$	$2.8^{+1.6}_{-1.7}$		0.061
AzTEC_J095913.99+023424.0		3.7	$4.7 \pm 1.3$	$2.8^{+1.5}_{-1.7}$		0.060
AzTEC_J100016.31+024715.8		3.7	$4.6 \pm 1.3$	$2.7^{+1.5}_{-1.8}$		0.067
AzTEC_J095951.72+024337.9 <sup>b,c</sup>		3.7	$4.4 \pm 1.2$	$2.6^{+1.5}_{-1.8}$		0.060
AzTEC_J095958.28+023608.2 <sup>b</sup>		3.6	$4.5 \pm 1.2$	$2.7^{+1.5}_{-1.8}$		0.069
AzTEC_J100031.06+022751.5 <sup>b</sup>		3.6	$4.9 \pm 1.3$	$2.7^{+1.6}_{-2.1}$		0.086
AzTEC_J095957.32+024141.4 <sup>b</sup>		3.6	$4.4 \pm 1.2$	$2.6^{+1.4}_{-1.7}$		0.068
AzTEC_J095930.47+023438.2 <sup>b,c</sup>		3.6	$4.5 \pm 1.2$	$2.6^{+1.5}_{-1.8}$		0.074
AzTEC_J100023.98+022950.0		3.6	$4.6 \pm 1.3$	$2.6^{+1.5}_{-1.9}$		0.080
AzTEC_J095920.64+023416.7 <sup>b</sup>		3.6	$4.5 \pm 1.2$	$2.6^{+1.5}_{-1.8}$		0.077
AzTEC_J095932.26+023649.5 <sup>b</sup>		3.6	$4.4 \pm 1.2$	$2.6^{+1.4}_{-1.8}$		0.075
AzTEC_J100000.79+022636.0		3.6	$4.6 \pm 1.3$	$2.6^{+1.5}_{-2.0}$		0.088
AzTEC_J095938.63+023146.2 <sup>b</sup>		3.6	$4.5 \pm 1.3$	$2.6^{+1.5}_{-1.9}$		0.086
AzTEC_J095943.74+023329.9 <sup>b,c</sup>		3.5	$4.4 \pm 1.3$	$2.5^{+1.5}_{-1.9}$		0.088
AzTEC_J100039.06+024128.6 <sup>b,c</sup>		3.5	$4.4 \pm 1.3$	$2.5^{+1.4}_{-1.9}$		0.089
AzTEC_J100012.42+022657.5		3.5	$4.5 \pm 1.3$	$2.5^{+1.4}_{-2.1}$		0.098
AzTEC_J100025.23+022608.0 <sup>a,d</sup>		3.3	$4.6 \pm 1.4$	$1.9^{+1.2}_{-2.0}$		0.144
AzTEC_J095939.01+022124.5 <sup>a,d</sup>		3.2	$6.5 \pm 2.0$	$1.3^{+0.5}_{-1.7}$		0.304

Notes: *a)* Sources have also been detected with Bolocam (J. Aguirre, private communication); *b)* AzTEC sources with one or more candidate MIPS 24  $\mu\text{m}$  counterpart (§ 6.3); *c)* AzTEC sources with one or more candidate radio counterpart (§ 6.2); *d)* These sources

the source population, we have verified that maximum likelihood flux densities derived from this approach differ by less than 0.7 mJy (i.e. well within the photometric error) for a variety of assumed models (e.g. single power law, Schechter function) and a wide range of parameters as measured from previous SCUBA, Bolocam, and MAMBO SMG surveys (Coppin et al. 2006; Laurent et al. 2005; Greve et al. 2004, , respectively).

We estimate the prior distribution of flux densities by generating 10,000 noiseless sky realisations, inserting sources with a uniform spatial distribution into a blank map with the source population described by Equation 4, where each source is described by the point source kernel. The pixel histogram of flux values from these sky maps gives an estimate of  $p(S_i)$ .

A plot of the PFD for a sample of the AzTEC source candidates is shown in Figure 6. These four sources represent the range of measured fluxes in the catalogue and demonstrate how the PFD varies according to the strength of the detection. Strictly speaking, the PFD for a given source candidate depends on both its detected flux *and* noise, but this translates into a dependence on  $S/N$  when the noise is uniform in the map, which is approximately true in this case. We calculate the de-boosted flux density for each source by locating the local maximum value of the PFD. These values are listed in column 5 of Table 1. The errors on the de-boosted fluxes shown in Table 1 represent the 68% confidence interval.

Using the PFD, we estimate the probability that each detected source candidate will be de-boosted to less than 0 mJy, which is listed in column 7 of Table 1 for each source candidate. Coppin et al. (2005, 2006) use these PFDs to exclude source candidates that have  $\geq 5\%$  probability of de-boosting to  $< 0$  as a way to limit the source list to candidates which have a higher probability of being real. While this may result in a source catalogue with fewer false-detections, it could exclude many real sources detected with low  $S/N$  and reduce the completeness of the source catalogue. Furthermore, while the de-boosted flux densities derived from the PFDs are not very sensitive to the assumed source population used to generate the prior distribution, the number of source candidates that meet the null threshold criterion is sensitive to the exact form of the prior. For these reasons, we choose to publish the entire list of  $\geq 3.5\sigma$  source candidates with the stipulation that some fraction of this catalogue (in particular, source candidates with  $S/N < 4$ ) represent false-detections, as addressed in § 5.2.

## 5.2 False-Detection Rate

Traditionally, a false-detection rate is the number of  $> N\sigma$  peaks caused purely by noise and therefore appear at locations where there are no real sources. However, in surveys such as ours, where the confused signal is significant relative to the noise, every pixel in the map is affected by the presence of sources. Therefore, the definition of false-detection rate becomes rather arbitrary. Another complication is that source confusion will increase the number of positive and negative peaks in a map, beyond the number found in our synthetic noise realisations. A common practise is to quote the false-detection rate as the number of *negative* peaks detected in the map with  $> N\sigma$  significance. However, it is

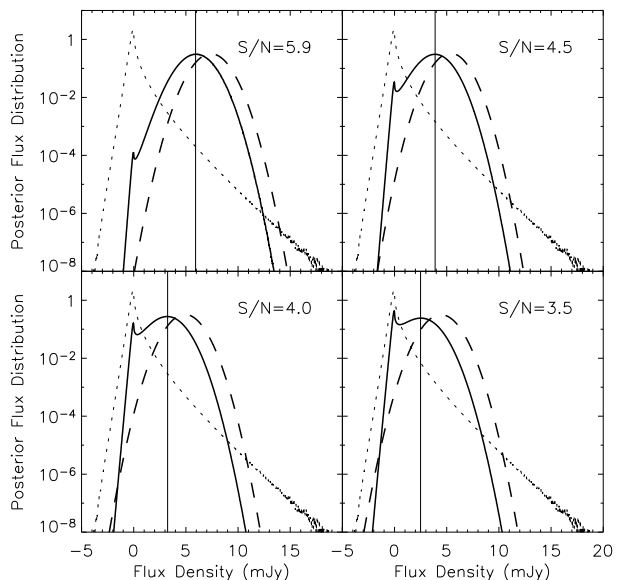


**Figure 6.** Posterior flux distributions (PFDs) for a sample of four AzTEC source candidates, whose  $S/N$  values are representative of the range observed in the entire source list. The dashed curve shows the Gaussian distribution assumed for the measured source flux distribution,  $p(S_m, \sigma_m | S_i)$ . The dotted curve is  $p(S_i)$ , estimated from simulated sky maps as described in § 5.1. The solid curve is the posterior flux distribution,  $p(S_i | S_m, \sigma_m)$ . All distributions have been normalised such that the integral under the curve is equal to 1. The vertical line indicates the local maximum of  $p(S_i | S_m, \sigma_m)$ , which gives the de-boosted flux density of the source listed in column 5 of Table 1.

difficult to interpret that number, mainly because source confusion may augment the number of negative peaks differently from the number of positive peaks.

Therefore, we show in Figure 7 the number of “sources” detected when the usual source finding algorithm is applied to our synthetic noise maps. These curves are proportional to the number of instances that a point with zero flux in a *noiseless, beam-convolved* map of the sky is detected above the given signal to noise ratio (or flux density). Because nearly half the points on a noiseless, beam-convolved map would have sub-zero flux (due to AC-coupling), the curves of Figure 7 give an upper limit to the number of such sub-zero points that would spuriously be called detections. Using this definition, the expected number of false-detections for AzTEC/COSMOS sources with  $S/N \geq 4.5$  is consistent with zero.

An alternative definition of false-detection rate could be the number of “source” detections at points on the noiseless, beam-convolved sky with intrinsic flux below  $S$ , where  $S$  could be the detection threshold of a follow-up observation, for instance with the SMA. But we refrain from such speculation here because the false-detection rate would depend on the source population as well as the rather arbitrary  $S$ .

## 5.3 Completeness

The differential completeness as a function of input source flux is shown in Figure 8. Completeness is estimated by in-

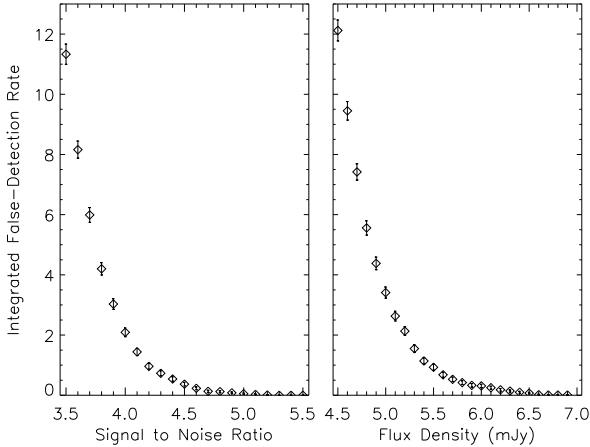


**Figure 7.** Number of expected false-detections in the AzTEC/COSMOS catalogue above a given signal to noise (left) and measured source flux (right). The false-detection rate determined here represents an upper limit to the real number of false-detections that we expect (see § 5.2).

jecting sources, one at a time, into the (sparsely populated) real signal map at random positions and checking if they are retrieved by our standard source identification algorithm. Adding one source at a time to the real signal map provides a valid estimate of the completeness because it 1) accounts for the effects of random and confusion noise present in the real map, 2) does not significantly alter the properties of the real map (only one source input at a time), and 3) is not dependent on a model of the source population (as is necessary for fully simulated data-sets using noise maps). We inject a total of 1,000 sources per flux value, ranging from 0.5–12 mJy in steps of 0.5 mJy. A source is considered to be recovered if it is detected with  $S/N \geq 3.5$  within  $10''$  of the input source position. We disregard any samples where the input source is injected (or retrieved) within  $10''$  of a real  $\geq 3.5\sigma$  source candidate in the map to avoid confusion with real sources. The AzTEC/COSMOS survey is 50% complete at 4 mJy, and 100% complete at 7 mJy.

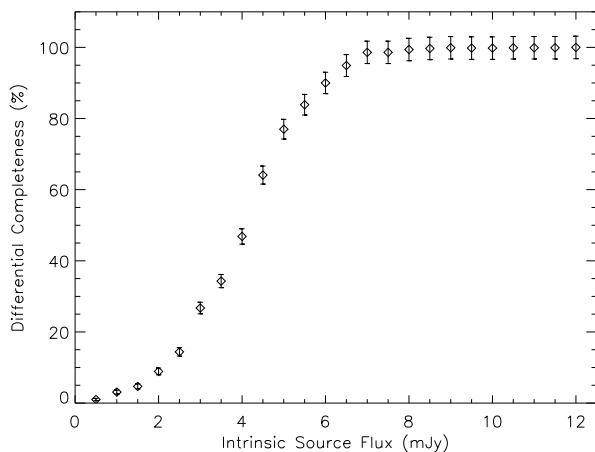


**Figure 8.** Differential completeness versus intrinsic source flux density. The errors are Poisson errors.

#### 5.4 Positional Uncertainty

The simulations described in § 5.3 offer a measure of the error on the position of sources identified in the AzTEC map due to the effects of both random and confusion noise. For the synthetic sources that are recovered, we calculate the distance between the input and output source positions and construct the probability,  $P(> D; S/N)$ , that an AzTEC source with signal to noise  $S/N$  will be detected outside a distance  $D$  of its true position. This positional uncertainty measurement is not sensitive to the contribution from positional errors arising from systematic and/or random errors introduced through corrections to the pointing model (§ 2.1). To account for this, we assume Gaussian random pointing errors of  $2''$  in both RA and DEC (see § 6.2 and Figure 11), and we generate 100 random variates for each recovered source to simulate pointing errors, which are added to the measured output source position. A plot of the positional uncertainty distribution as a function of distance for three different signal to noise bins is shown in Figure 9. For all  $\geq 3.5\sigma$  AzTEC source candidates, the probability that an AzTEC source will be detected within  $4.5''$  of its true position is  $\geq 80\%$ .

## 6 COMPARISON WITH OTHER CATALOGUES

A detailed multi-wavelength study of AzTEC/COSMOS sources will be deferred to Paper III. In this section, we discuss the confirmations of AzTEC sources with observations by Bolocam, identify potential radio and MIPS  $24 \mu\text{m}$  counterparts to the mm sources, and study the faint mm emission from the rest of the radio/IR population.

### 6.1 AzTEC Overlap with Bolocam Sources

The AzTEC/COSMOS field overlaps slightly with the larger, shallower Bolocam/COSMOS survey. Two of our high-significance source candidates lie within  $4''$  of Bolocam-identified sources detected with  $S/N \geq 3.5$ , confirming the

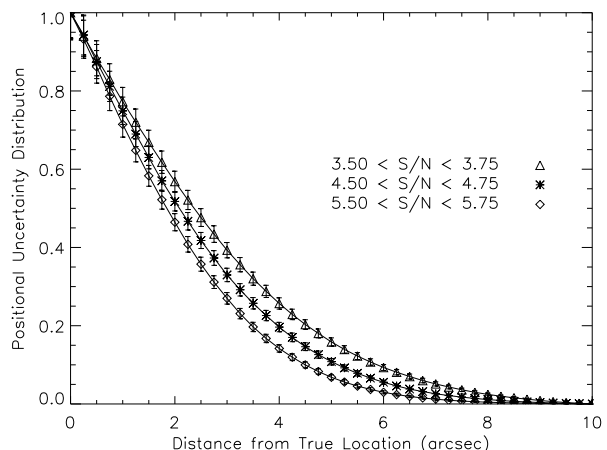


**Figure 9.** The positional uncertainty distribution,  $P(> D; S/N)$ , for three sample signal to noise bins, showing the probability that an AzTEC source detected at a signal to noise ratio of  $S/N$  will lie outside a distance  $D$  from its true position.

reality of these sources (J. Aguirre, private communication). The third Bolocam source that lies within the AzTEC 75% uniform coverage region is not detected in our survey.

Two additional Bolocam-detected sources lie within the 25% uniform coverage region of the AzTEC map (the 2.5 mJy/beam contour shown in Figure 2). We tentatively confirm these two Bolocam sources at the  $\sim 3\sigma$  level. Though located 17–18'' from the Bolocam centroid, these AzTEC source candidates are within the 95% confidence radius of the positional error in the Bolocam/COSMOS survey (J. Aguirre, private communication). These four AzTEC sources which are coincident with Bolocam detections are identified in Table 1.

## 6.2 The Corresponding Radio Population

The identification of radio counterparts has often been used to improve on the positional uncertainty of SMGs (e.g., Ivison et al. 2002, 2007; Chapman et al. 2003, 2005; Pope et al. 2005, 2006). For this comparison we use the 4.5 $\sigma$  catalogue from the VLA/COSMOS survey (Schinnerer et al. 2007), which has a  $1\sigma$  depth of 10.5  $\mu$ Jy rms. To identify potential radio counterparts to our mm-identified sources, we use a conservatively large search radius of 9'' from the measured AzTEC source position. If we assume that the location of a candidate radio counterpart is the true location of a given AzTEC source, then the probability that we detect the AzTEC source at a distance greater than 9'' from the radio source is given by the positional uncertainty distribution that was calculated in § 5.4,  $P(> 9''; S/N)$ , which is  $\leq 1\%$  for all  $S/N$  values  $\geq 3.5$ . Thus using a search radius of 9'' makes it unlikely that we would fail to identify the radio counterpart to an AzTEC source candidate, should it exist. On the other hand, if the radio number density is high enough, we will expect some fraction of false associations with AzTEC galaxies. We quantify this through the ‘‘P-statistic’’, which gives the probability that the first nearest neighbour radio source will lie within a distance  $\theta$  from a given point and is given by

$$P(\theta) = 1 - e^{-n\pi\theta^2} \quad (5)$$

where  $n$  is the number density of radio sources (e.g., Scott & Tout 1989). This P-statistic is equivalent to the probability that a radio source will lie within a distance  $\theta$  of an AzTEC source candidate by chance. Assuming uniform density (i.e. no clustering) of radio sources,  $n = 2350 \text{ deg}^{-2}$  in this field, and thus  $P(9'') = 4.5\%$ . Hence we expect 4.5% of radio sources identified within 9'' of an AzTEC source candidate to be false associations.

For the list of source candidates in Table 1, 15 have a single radio counterpart within 9'' of the AzTEC source position, and 3 have two radio sources within 9'' of the AzTEC source position. AzTEC sources with at least one candidate radio counterpart are identified in Table 1. From the P-statistic, we expect one of these 18 to be a false association. However, we may expect more false associations than this if radio sources cluster on scales smaller than 9'', making the local P-statistic in the neighbourhood of mm sources higher. The fraction of AzTEC sources with potential radio counterparts (36%) is consistent with that found in the SCUBA/SHADES survey (Ivison et al. 2007)

of 30–50%, assuming the same limiting flux (45  $\mu$ Jy at 1.4 GHz), but is only marginally consistent (within  $2\sigma$ , Poisson errors) with that of the MAMBO/COSMOS survey (Bertoldi et al. 2007) of 67%. Given the depth of the radio survey from Bertoldi et al. (2007, 7–8  $\mu$ Jy), this may simply reflect the relative completeness in the different radio catalogues. Our radio fraction could also be diluted by including low  $S/N$  AzTEC sources, which have a higher number of false-detections. The fraction of AzTEC  $\geq 4\sigma$  sources (only 2 false-detections expected) with candidate radio counterparts is 12/27 (44%) and agrees with the Bertoldi et al. (2007) radio fraction within  $1\sigma$ .

We use the same radio catalogue to explore the weaker, confused population of SMGs in the AzTEC map. Figure 10 (left panel) shows the results of averaging the AzTEC map flux in  $2' \times 2'$  postage stamps extracted from regions centred at the 598 radio source positions that lie within the AzTEC map boundary. Since we compute a weighted average for each pixel, we extend this analysis to the noisier edges of the mm map (10% coverage region, with an area of 0.28  $\text{deg}^2$ ). All radio sources that have candidate AzTEC counterparts detected at  $\geq 3.5\sigma$  or  $\leq -3.5\sigma$  have been excluded in order to restrict this analysis to radio sources with faint AzTEC emission, below the  $S/N$  threshold used for discrete source identification. The 8.06 $\sigma$  stacked signal implies a mean 1.1 mm flux of  $487 \pm 60 \mu\text{Jy}$  for the radio sources in the catalogue. No significant difference in the average 1.1 mm flux is detected when we stack separately on two groups of radio sources divided by their 1.4 GHz flux. For radio sources with flux density  $> 66 \mu\text{Jy}$  (293/598), the stacked 1.1 mm signal is  $530 \pm 87 \mu\text{Jy}$ , while the stacked 1.1 mm flux for radio sources  $\leq 66 \mu\text{Jy}$  (305/598) is  $465 \pm 84 \mu\text{Jy}$ . These values differ by only 13% and agree within the errors.

In the top right panel of Figure 10, we show a histogram of the 1.1 mm  $S/N$  ratio at the location of all 598 radio sources. For comparison, we generate 100 fake catalogues, each with 598 positions chosen randomly across the AzTEC map, and construct the histogram of AzTEC  $S/N$  ratio at these locations. Since these positions were chosen at random, we expect that the distribution of  $S/N$  values should be nearly symmetric about zero. The bottom right panel of Figure 10 shows the difference between the histogram of the  $S/N$  ratios at the radio source positions and that at the random positions. This clearly demonstrates that there is a significant contribution to the stacked flux image from low  $S/N$  mm sources. Roughly 1/2 of the stacked signal arises from sources with  $S/N < 1.8$  that fall below the detection threshold for source identification. This analysis demonstrates that the AzTEC map is sensitive to very faint millimetre emission down to flux levels on order of the  $1\sigma$  rms of the map.

The radio source stacking analysis can also be used to estimate the residual systematic and rms pointing errors in the AzTEC map due to errors in the astrometry. The stacked signal peaks at  $(\Delta\text{RA}, \Delta\text{DEC}) = (0.4'', -2.1'')$ , indicating a potential small systematic offset. Noise in the pointing solution leads to a broadening of the stacked signal, and so we use a measure of this broadening to determine the rms pointing uncertainty of our AzTEC observations. The model is as follows: assuming that the pointing errors are random and Gaussian distributed with mean zero and standard deviation  $\sigma_p$ , the stacked AzTEC flux should be equal to the

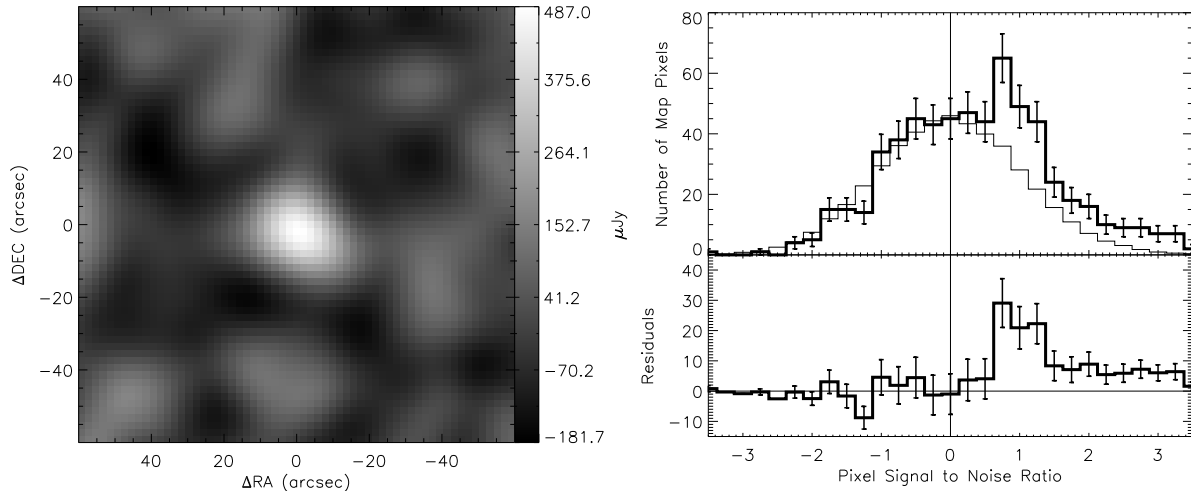


**Figure 10.** **Left:** Average AzTEC map flux in  $2' \times 2'$  cutouts centred at the 598 radio source positions. We have excluded the positions of radio sources that are located within  $9''$  of AzTEC peaks with  $|S/N| \geq 3.5$ . **Top Right:** Histogram of the signal to noise ratio of the 1.1 mm map at the radio source positions (thick line) versus that at positions chosen randomly in the map (thin line). **Bottom Right:** The difference between the two histograms above.

convolution of a Gaussian (with standard deviation  $\sigma_p$ ) with the point source kernel. We calculate the cross-correlation of the stacked AzTEC flux at the radio source locations with this model, varying  $\sigma_p$ . We find that for all values of  $\sigma_p$ , the maximum value of the cross-correlation matrix is at an offset of zero in RA and  $-2''$  in DEC, consistent with a small systematic pointing offset. Figure 11 shows the value of the maximum correlation as a function of pointing uncertainty,  $\sigma_p$ . The strongest correlation occurs for  $\sigma_p = 0.89''$ . However, the curve becomes very flat at  $\sigma_p < 2''$  because the stacked image itself is limited to  $2''$  pixelization. Also, if radio sources in the COSMOS field cluster on scales  $< 2''$ , this would also broaden the width of the stacked signal, further complicating this estimate. Though we cannot accurately measure the value of  $\sigma_p$  with this technique when  $\sigma_p$  is small, we can state with confidence that  $\sigma_p < 2''$ , and we adopt this as a conservative estimate of the error in the astrometry in our map. We combine this error with the measured distances between input and output source positions as described in § 5.4 to determine the positional uncertainty distribution shown in Figure 9.

### 6.3 Coincident $24 \mu\text{m}$ Detections

A similar comparison can be made to sources detected at  $24 \mu\text{m}$  by the *Spitzer*/MIPS instrument in the COSMOS deep survey (Sanders et al. 2007). There are 2082  $24 \mu\text{m}$  sources with  $S/N \geq 5$  ( $S_{24\mu\text{m}} \geq 60 \mu\text{Jy}$ ) within the 75% uniform coverage region of the AzTEC/COSMOS map, and 49/50 AzTEC source candidates within the coverage of the MIPS  $24 \mu\text{m}$  image. Of these, 30 individual  $24 \mu\text{m}$  sources are found within  $9''$  of an AzTEC source, while 2 AzTEC sources have two  $24 \mu\text{m}$  sources within a  $9''$  radius. AzTEC sources with one or more potential MIPS  $24 \mu\text{m}$  counterparts are identified in Table 1. The

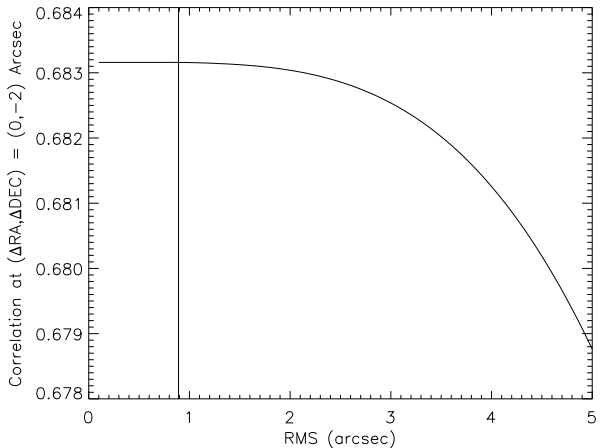


**Figure 11.** Amplitude of the cross-correlation between the map in Figure 10 and a map constructed by convolving the point source kernel with a Gaussian with standard deviation  $\sigma_p$ . For all values of  $\sigma_p$ , the maximum correlation occurs at  $(\Delta\text{RA}, \Delta\text{DEC}) = (0'', -2'')$ .

source density of  $24 \mu\text{m}$  sources in this field is quite large ( $14280 \text{ deg}^{-2}$ ) and the probability of chance coincidence within  $9''$  is 24.5%, so we expect 12 false associations. As shown in Younger et al. (2007), it is not uncommon to find an unrelated  $24 \mu\text{m}$  source within  $9''$  of an SMG. We therefore do not use the  $24 \mu\text{m}$  catalogue as a signpost for mm-wavelength emission. A summary of the number of AzTEC source candidates with potential radio and  $24 \mu\text{m}$  counterparts is given in Table 2. A detailed multi-wavelength study of the AzTEC sources in this field will be presented in Paper III.

We perform the same stacking analysis as done for the

	AzTEC source candidates with $\geq 1$ counterpart	AzTEC source candidates with 2 counterparts	$P(9'')$	Catalogue Completeness
Radio	18/50 (36%)	3/50 (6%)	4.5%	$4\sigma=45\mu\text{Jy}$
24 $\mu\text{m}$	32/49 (65%)	2/49 (4%)	24.5%	$5\sigma=60\mu\text{Jy}$

**Table 2.** Comparison of AzTEC source candidates with radio and MIPS 24  $\mu\text{m}$  sources, using a search radius of  $9''$ .  $P(9'')$  is the probability of a chance coincidence within the  $9''$  search radius.

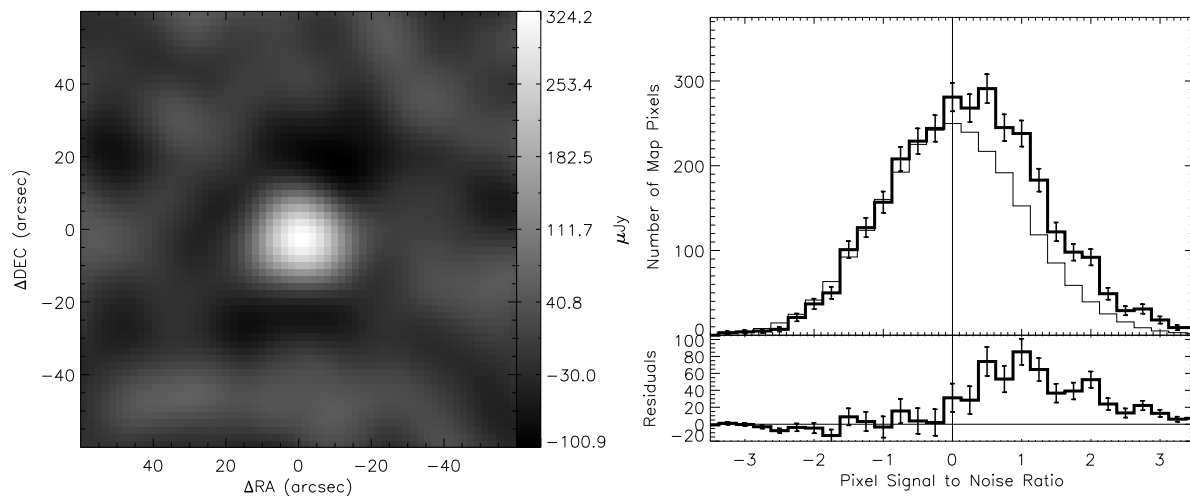


**Figure 12.** **Left:** Average AzTEC map flux in  $2' \times 2'$  cutouts centred at 3129 24  $\mu\text{m}$  source positions. We have excluded the positions of 24  $\mu\text{m}$  sources that are located within  $9''$  of AzTEC peaks with  $|S/N| \geq 3.5$ . **Top Right:** Histogram of the signal to noise ratio of the 1.1 mm map at the 24  $\mu\text{m}$  source positions (thick line) versus that at positions chosen randomly in the map (thin line). **Bottom Right:** The difference between the two histograms above.

radio catalogue on the 24  $\mu\text{m}$  catalogue. The results are shown in Figure 12. Again, MIPS sources within  $9''$  of an AzTEC pixel with  $S_{1.1\text{mm}} \geq 3.5\sigma$  or  $S_{1.1\text{mm}} \leq -3.5\sigma$  have been excluded. This leaves 3129 MIPS sources within the extended AzTEC map. The stacked signal strength is  $12.8\sigma$ , and the mean 1.1 mm flux of these sources is  $324 \pm 25 \mu\text{Jy}$ . A histogram of the 1.1 mm  $S/N$  ratio at the location of all 3129 MIPS 24  $\mu\text{m}$  sources is shown in the right panel of Figure 12, demonstrating that the stacked signal is dominated by low ( $< 2\sigma$ )  $S/N$  mm sources.

## 7 THE CONTRIBUTION OF AZTEC SOURCES IN COSMOS TO THE COSMIC INFRARED BACKGROUND

Using the de-boosted 1.1 mm AzTEC flux densities derived from the PFDs, we sum the flux densities of the  $\geq 3.5\sigma$  source candidates to determine the resolved fraction of the Cosmic Infrared Background (CIB) in this survey. An integrated flux of  $1.3 \text{ Jy deg}^{-2}$  from those galaxies in the AzTEC catalogue (Table 1) is compared to 18–24  $\text{Jy deg}^{-2}$  from the CIB measured by *COBE*-FIRAS at 1.1 mm (Puget et al. 1996; Fixsen et al. 1998), demonstrating that we have resolved 5.3–7.1% of the CIB into bright

millimetre-wavelength sources in the COSMOS field. This value is an overestimate of the real CIB resolved in this study because at least some of the source candidates are false-detections (random noise peaks). Also, there appears to be an over-density of bright mm sources in this field, in which case the local CIB would be larger than the average value measured in Puget et al. (1996) and Fixsen et al. (1998).

Furthermore, we can estimate the fraction of the millimetre CIB resolved by the entire radio population in the COSMOS field. Using the stacked analysis described in § 6.2, we first calculate the average millimetre flux of the faint AzTEC sources with  $S/N < 3.5$  that are associated with the 598 radio counterparts distributed over  $0.28 \text{ deg}^2$ , which is  $487 \pm 60 \mu\text{Jy}$  at 1.1 mm, or  $1.0 \pm 0.1 \text{ Jy deg}^{-2}$ . This resolved fraction of 4.3–5.7% of the millimetre CIB is comparable to that measured from stacking the 850  $\mu\text{m}$  flux at the position of 1.4 GHz radio sources in the SCUBA/GOODS-N field, where Wang et al. (2006) resolve 3.4–4.8% of the CIB (excluding the contribution from  $\geq 4\sigma$  sources) using a radio catalogue with a similar limiting flux ( $40 \mu\text{Jy}$ ) as the COSMOS radio catalogue. Next we add the contribution of  $0.46 \text{ Jy deg}^{-2}$  at 1.1 mm from the 18 bright ( $S/N \geq 3.5$ ) AzTEC sources in Table 1 that have radio counterparts. We therefore conclude that our AzTEC map has resolved a total

1.1 mm flux of  $1.46 \text{ deg}^{-2}$ , or  $7 \pm 1\%$  of the CIB, due to the full population of radio sources in COSMOS.

Finally, considering the average millimetre flux of the faint population ( $< 3.5\sigma$ ) of AzTEC galaxies at the positions of the MIPS 24  $\mu\text{m}$  sources (§ 6.3), we estimate a total 1.1 mm flux of  $4.4 \pm 0.3 \text{ Jy deg}^{-2}$ , thereby resolving 18.3–24.4% of the CIB. Similarly Wang et al. (2006) resolve 13.4–19.0% of the CIB from their 850  $\mu\text{m}$  stacking analysis of MIPS 24  $\mu\text{m}$  sources in the SCUBA/GOODS-N map. Although their 24  $\mu\text{m}$  catalogue is slightly shallower than the COSMOS MIPS 24  $\mu\text{m}$  source catalogue (80  $\mu\text{Jy}$  and 60  $\mu\text{Jy}$ , respectively), these CIB fractions agree within the errors of the measurements.

## 8 CONCLUSIONS

We have imaged a  $0.15 \text{ deg}^2$  region within the COSMOS field with AzTEC, a new mm-wavelength camera, with uniform sensitivity of 1.3 mJy/beam at 1.1 mm. We have identified 50 source candidates in the AzTEC/COSMOS map with signal to noise ratio  $\geq 3.5$ , 16 of which are detected with  $S/N \geq 4.5$ , where the expected number of false-detections is zero. Seven of the  $\geq 5\sigma$  source candidates have been followed up and confirmed with SMA imaging (Younger et al. 2007). The sources are spread throughout the field, with only 3 located in the  $z = 0.73$  cluster environment. Our catalogue is 50% complete at an intrinsic flux density of 4 mJy, and is 100% complete at 7 mJy. The positional uncertainty of these AzTEC sources due to random and confusion noise is determined through simulations which show that sources with  $S/N \geq 3.5$  have  $\geq 80\%$  probability of being detected within  $4.5''$  of their true location.

Comparing our  $\geq 3.5\sigma$  source candidate list with the radio source catalogue of Schinnerer et al. (2007), we find that the fraction of AzTEC sources with potential radio counterparts is 36% and is consistent with that found in the SCUBA/SHADES survey (Ivison et al. 2007) at similar flux levels. From averaging the AzTEC map flux at the locations of the radio and MIPS 24  $\mu\text{m}$  (Sanders et al. 2007) source positions, we statistically detect the faint mm emission (below our detection threshold) of radio and MIPS 24  $\mu\text{m}$  sources and thereby demonstrate that errors in the mean astrometry of our map arising from the pointing model are small ( $< 2''$ ). Estimates of the resolved fraction of the millimetre CIB due to these radio and mid-IR galaxy populations is  $7 \pm 1\%$  and  $21 \pm 3\%$  respectively.

The AzTEC/COSMOS field samples a region of high galaxy over-density compared to the regions imaged with MAMBO and Bolocam, and our AzTEC/COSMOS map contains a large number of very bright mm sources (9 with corrected flux density  $\geq 5 \text{ mJy}$ , where 4–5 are expected for an unbiased field). We will present a complete analysis of the relationship between the SMG population and the foreground galaxy population in Paper II of this series.

The availability of extensive high quality multi-wavelength data from the radio to the X-ray makes the follow-up analysis of the detected sources readily possible and will allow us to study the nature of these sources. A full analysis of the multi-wavelength properties of the sources detected in this survey will be presented in Paper III.

## ACKNOWLEDGEMENTS

The authors are grateful to J. Aguirre, J. Karakla, K. Soucar, I. Coulson, R. Tilanus, R. Kackley, D. Haig, S. Doyle, J. Lowenthal, and the observatory staff at the JCMT who made these observations possible. Support for this work was provided in part by the NSF grant AST 05-40852 and the grant from the Korea Science & Engineering Foundation (KOSEF) under a cooperative Astrophysical Research Center of the Structure and Evolution of the Cosmos (ARCSEC). IA and DHH acknowledge partial support by CONACyT from research grants 39953-F and 39548-F. This research has made use of the NASA/IPAC Extragalactic Database (NED) which is operated by the Jet Propulsion Laboratory, California Institute of Technology, under contract with the National Aeronautics and Space Administration.

## REFERENCES

- Barger A. J., Cowie L. L., Sanders D. B., Fulton E., Taniguchi Y., Sato Y., Kawara K., Okuda H., 1998, *Nature*, 394, 248
- Bertoldi F., Carilli C., Aravena M., Schinnerer E., Voss H., Smolcic V., Jahnke K., Scoville N., Blain A., Menten K. M., et al., 2007, *ApJS*, 172, 132
- Borys C., Chapman S., Halpern M., Scott D., 2003, *MNRAS*, 344, 385
- Chapman S. C., Blain A. W., Ivison R. J., Smail I. R., 2003, *Nature*, 422, 695
- Chapman S. C., Blain A. W., Smail I., Ivison R. J., 2005, *ApJ*, 622, 772
- Chapman S. C., Scott D., Borys C., Fahlman G. G., 2002, *MNRAS*, 330, 92
- Coppin K., Chapin E. L., Mortier A. M. J., Scott S. E., Borys C., Dunlop J. S., Halpern M., Hughes D. H., Pope A., Scott D., et al., 2006, *MNRAS*, 372, 1621
- Coppin K., Halpern M., Scott D., Borys C., Chapman S., 2005, *MNRAS*, 357, 1022
- Fixsen D. J., Dwek E., Mather J. C., Bennett C. L., Shafer R. A., 1998, *ApJ*, 508, 123
- Glenn J., Bock J. J., Chattopadhyay G., Edgington S. F., Lange A. E., Zmuidzinas J., Mauskopf P. D., Rownd B., Yuen L., Ade P. A., 1998, in Phillips T. G., ed., *Proc. SPIE, Advanced Technology MMW, Radio, and Terahertz Telescopes Vol. 3357, Bolocam: a millimeter-wave bolometric camera*. pp 326–334
- Greve T. R., Ivison R. J., Bertoldi F., Stevens J. A., Dunlop J. S., Lutz D., Carilli C. L., 2004, *MNRAS*, 354, 779
- Griffin M. J., Orton G. S., 1993, *Icarus*, 105, 537
- Haig D. J., Ade P. A. R., Aguirre J. E., Bock J. J., Edgington S. F., Enoch M. L., Glenn J., Goldin A., Golwala S., Heng K., et al., 2004, in Holland W. S., Zmuidzinas J., Withington S., eds, *Proc. SPIE, Millimeter and Submillimeter Detectors for Astronomy II Vol. 5498, Bolocam: status and observations*. pp 78–94
- Hogg D. W., Turner E. L., 1998, *PASP*, 110, 727
- Holland W. S., Robson E. I., Gear W. K., Cunningham C. R., Lightfoot J. F., Jenness T., Ivison R. J., Stevens J. A., Ade P. A. R., Griffin M. J., et al., 1999, *MNRAS*, 303, 659

- Hughes D. H., Serjeant S., Dunlop J., Rowan-Robinson M., Blain A., Mann R. G., Ivison R., Peacock J., Efstathiou A., Gear W., et al., 1998, *Nature*, 394, 241
- Ivison R. J., Greve T. R., Dunlop J. S., Peacock J. A., Egami E., Smail I., Ibar E., van Kampen E., Aretxaga I., Babbedge T., et al., 2007, *MNRAS*, 380, 199
- Ivison R. J., Greve T. R., Smail I., Dunlop J. S., Roche N. D., Scott S. E., Page M. J., Stevens J. A., Almaini O., Blain A. W., et al., 2002, *MNRAS*, 337, 1
- Kennicutt Jr. R. C., 1998, *ARA&A*, 36, 189
- Kreysa E., Gemuend H.-P., Gromke J., Haslam C. G., Reichertz L., Haller E. E., Beeman J. W., Hansen V., Sievers A., Zylka R., 1998, in Phillips T. G., ed., *Proc. SPIE, Advanced Technology MMW, Radio, and Terahertz Telescopes Vol. 3357, Bolometer array development at the Max-Planck-Institut fuer Radioastronomie*. pp 319–325
- Laurent G. T., Aguirre J. E., Glenn J., Ade P. A. R., Bock J. J., Edgington S. F., Goldin A., Golwala S. R., Haig D., Lange A. E., et al., 2005, *ApJ*, 623, 742
- Mortier A. M. J., Serjeant S., Dunlop J. S., Scott S. E., Ade P., Alexander D., Almaini O., Aretxaga I., Baugh C., Benson A. J., et al., 2005, *MNRAS*, 363, 563
- Pope A., Borys C., Scott D., Conselice C., Dickinson M., Mobasher B., 2005, *MNRAS*, 358, 149
- Pope A., Scott D., Dickinson M., Chary R.-R., Morrison G., Borys C., Sajina A., Alexander D. M., Daddi E., Frayer D., et al., 2006, *MNRAS*, 370, 1185
- Puget J.-L., Abergel A., Bernard J.-P., Boulanger F., Burton W. B., Desert F.-X., Hartmann D., 1996, *A&A*, 308, L5+
- Sanders D. B., Mirabel I. F., 1996, *ARA&A*, 34, 749
- Sanders D. B., Salvato M., Aussel H., Ilbert O., Scoville N., Surace J. A., Frayer D. T., Sheth K., Helou G., Brooke T., et al., 2007, *ApJS*, 172, 86
- Schinnerer E., Smolčić V., Carilli C. L., Bondi M., Ciliegi P., Jahnke K., Scoville N. Z., Aussel H., Bertoldi F., Blain A. W., et al., 2007, *ApJS*, 172, 46
- Scott D., Tout C. A., 1989, *MNRAS*, 241, 109
- Scott S. E., Dunlop J. S., Serjeant S., 2006, *MNRAS*, 370, 1057
- Scott S. E., Fox M. J., Dunlop J. S., Serjeant S., Peacock J. A., Ivison R. J., Oliver S., Mann R. G., Lawrence A., Efstathiou A., et al., 2002, *MNRAS*, 331, 817
- Scoville N., Aussel H., Benson A., Blain A., Calzetti D., Capak P., Ellis R. S., El-Zant A., Finoguenov A., Giavalisco M., et al., 2007, *ApJS*, 172, 150
- Scoville N., Aussel H., Brusa M., Capak P., Carollo C. M., Elvis M., Giavalisco M., Guzzo L., Hasinger G., Impey C., et al., 2007, *ApJS*, 172, 1
- Smail I., Ivison R. J., Blain A. W., 1997, *ApJ*, 490, L5+
- Smail I., Ivison R. J., Blain A. W., Kneib J.-P., 1998, *ApJ*, 507, L21
- Smail I., Ivison R. J., Blain A. W., Kneib J.-P., 2002, *MNRAS*, 331, 495
- Wang W.-H., Cowie L. L., Barger A. J., 2006, *ApJ*, 647, 74
- Wilson G. W., Austermann J. E., Perera T. A., Scott K. S., Ade P. A. R., Bock J. J., Glenn J., Golwala S. R., Kim S., Kang Y., et al., 2008, *MNRAS*, submitted
- Younger J. D., Fazio G. G., Huang J.-S., Yun M. S., Wilson G. W., Ashby M. L. N., Gurwell M. A., Lai K., Peck A. B., Petitpas G. R., et al., 2007, *ArXiv e-prints*, 708